J Appl Physiol
91: 459–473, 2001.

α-Actin: disposition, quantities, and estimated effects on lung recoil and compliance

E. H. OLDMIXON,[1] K. CARLSSON,[2] C. KUHN III,[1] J. P. BUTLER,[3] AND F. G. HOPPIN, JR.[1]
[1]*Departments of Medicine and Pathology, Memorial Hospital of Rhode Island and Brown University, Pawtucket, Rhode Island 02860;* [2]*Biomedical and X-ray Physics, Royal Institute of Technology, Stockholm, SE-10044 Sweden; and* [3]*Physiology Program, Harvard School of Public Health, Boston, Massachusetts 02114*

Received 2 June 2000; accepted in final form 7 February 2001

Oldmixon, E. H., K. Carlsson, C. Kuhn III, J. P. Butler, and F. G. Hoppin, Jr. α-Actin: disposition, quantities, and estimated effects on lung recoil and compliance. *J Appl Physiol* 91: 459–473, 2001.—We have investigated the basis and implications of pneumoconstriction by measuring disposition and quantities of α-smooth muscle actin in rat and guinea pig lungs and modeling its effects on lung recoil and compliance. A robust marker of contractility, α-smooth muscle actin appears in smooth muscle or myofibroblast-like cells in pleura, airways, blood vessels, and alveolar ductal tissues. In each site, we measured its transected area by immunofluorescent staining and frequency-modulated scanning confocal microscopy. We incorporated these data in a model of the parenchyma consisting of an extensive elastic network with embedded contractile structures. We conclude that contraction at any one of these sites alone can decrease parenchymal compliance by 20–30% during tidal breathing. This is due mostly to the stiffness of activated contractile elements undergoing passive cycling; constant muscle tension would have little effect. The magnitude of the effect corresponds with known responses of the lung to hypocapnia, consistent with a homeostatic function in which gas exchange is defended by redistributing ventilation away from overventilated units.

alveolar duct; intensity-modulated multiple-wavelength scanning confocal microscopy; lung compliance; ventilation-perfusion ratio; hypocapnia

A VARIETY OF CONSTRICTING AGENTS can increase the lung's elastic recoil pressure and elastance (3, 6, 7, 25, 30, 42), and conversely relaxing agents can decrease its elastic recoil pressure (9). The static and passive dynamic properties of strips cut from lung parenchyma are influenced by smooth muscle agonists (10, 17, 32, 38, 50). Hypocapnia can reduce the lung's dynamic compliance on the order of 30% (1, 18, 41, 43, 48, 49), and this may represent a mechanism for control of ventilation (6, 18).

The source of this contractility, however, is unclear. Structural considerations suggest that contractile elements in the airways, blood vessels, or alveolar ducts can draw in on the surrounding parenchyma, thereby increasing its tensions. Contractile interstitial cells located within the alveolar walls themselves might increase the tensions of the alveolar parenchyma (19, 50). Airways acting alone may have an effect, because selective pharmacological constriction of conducting airways substantially reduces quasi-static and dynamic lung compliances (30). Other locations may also have independent effects, because agonists can change tissue dynamic properties independently of airway resistance (17). Furthermore, it has been argued that the contractility observed in subpleural strips of lung parenchyma may not be due to vascular or airway smooth muscle contraction (10, 19, 38).

We thought that some insight might be gained from knowing more about the contractile material in each location and estimating the effects of each on lung recoil and compliance. Accordingly, we chose α-smooth muscle actin as a major marker of contractile capability, and we applied a variety of microscopic techniques to sections of rat and guinea pig lungs to characterize the cells that contained it and to determine its locations and quantities in the lung parenchyma. We then modeled its effects by considering the lung parenchyma as an elastic network with embedded contractile elements. In the model, the elastic network was given the known elastic properties of relaxed lung, and the contractile elements were given the plastoelastic properties of passively cycled, activated smooth muscle. This model, incorporating the anatomical data from the first part of the study, estimates the effects of activation of the contractile elements in each location on regional parenchymal recoil and compliance during tidal breathing.

Our results show, in the two species examined, that any one of the locations alone has sufficient contractile material to account for modest but significant reduction of parenchymal compliance under dynamic conditions. This is consistent with the hypothesis that this mechanism, locally responsive to carbon dioxide levels, defends the overall efficiency of gas exchange by modulating local ventilation-perfusion ($\dot{V}/\dot{Q}$) ratios.

Address for reprint requests and other correspondence: F. G. Hoppin, Jr., Division of Pulmonary and Critical Care Medicine, Memorial Hospital of Rhode Island, 111 Brewster St., Pawtucket, RI 02860 (E-mail: frederic_hoppin_jr@brown.edu).

The costs of publication of this article were defrayed in part by the payment of page charges. The article must therefore be hereby marked "*advertisement*" in accordance with 18 U.S.C. Section 1734 solely to indicate this fact.

Glossary

Primary symbols

FORCES

F	force
T	tension (force per length)
P	pressure (force per area)
σ	nominal stress (force per area at l_o)

DIMENSIONS

A	area
V	volume
ρ	density of embedded structure in the lung unit
TLC	maximal physiological lung unit volume
FRC	relaxed physiological lung unit volume

MECHANICAL PROPERTIES

κ	bulk modulus
μ	shear modulus
l_o	length for maximal muscle stress

GEOMETRY

θ	angle of muscle fiber to the axis of airway cylinder or equator of ductal sphere
a	radius of sphere or cylinder
u	displacement of a boundary

Modifiers

GEOMETRY

ax	axial
circ	circumferential
tm	transmural
1	inner radius of surrounding (thick-walled) parenchyma, or equivalently outer radius of (thin-walled) duct or airway
2	outer radius of lung unit

STRUCTURES

ce	contractile element
tiss	tissue
L	lung
duct	alveolar duct
aw	airway
par	parenchyma
pl	pleura

CONDITION

active	contractile elements activated
passive	contractile elements relaxed

METHODS

Immunostaining

We used a monoclonal antibody to mark α-smooth muscle actin (44). It is highly specific, having been raised against the highly conserved amino terminal 10 amino acids of the smooth muscle isoform of α-actin. It is nonetheless very broad in its species reactivity, including human, rat, and chicken (44), cow, frog, goat, guinea pig, mouse, rabbit, dog, sheep, and snake (Sigma Chemical), and hamster and pig (personal observations of an author, C. Kuhn III).

The antibody was visualized by three different techniques. *1*) To determine the disposition of α-smooth muscle actin on large sections with moderately well preserved septal configuration, we examined frozen sections by transmission light microscopy with the antibody made visible by diaminobenzidine-horseradish peroxidase (DAB-HRP). *2*) To quantify α-smooth muscle actin in various sites over large fields of view, we prepared paraffin sections and used intensity-modulated multiple-wavelength scanning confocal microscopy (IMS) to measure the areas of fluorescence of Cy-3 linked to the antibody and to obtain anatomical context from fluorescent images of BODIPY-SE (Molecular Probes, Eugene, OR) staining lung tissue generally. *3*) To determine the subcellular patterns and concentrations of α-smooth muscle actin, we examined epoxy sections by transmission electron microscopy with the antibody visualized by immunogold.

Organ Isolation, Fixation, and Sample Preparation

Experimental animals comprised six female, viral antigen-free Sprague-Dawley rats (241–348 g) and three guinea pigs (423–523 g). Each was briefly sedated with carbon dioxide (dry ice vapor in a desiccator) and then anesthetized with pentobarbital sodium (30–41.5 mg/kg body wt im). Tracheal intubation was immediately performed, and the animal was maintained on a ventilator until the heart and lungs could be rapidly removed en bloc.

Transmission light microscopy. Rat lungs were filled with a 1:1 mixture of cryostabilizing compound (Tissue-Tek OCT compound; Sakura Finetek, Torrance, CA) and saline. Blocks of tissue were placed in pools of OCT compound on copper chucks and frozen by immersion in 2-methyl butane cooled in dry ice. Frozen sections were prepared on a cryotome with section thickness of 6 μm. Sections were thaw-mounted on silanized slides and dried for 30–60 min. After fixation for 5 min in 80% ethanol, the sections were hydrated in phosphate buffered saline-horse serum albumin-horse serum and incubated with anti-α-smooth muscle actin antibody 1:1,000 for 1 h. The bound antibody was visualized by an immunoperoxidase reaction by using the avidin-biotin complex method with commercial kits (Vectastain, Vector Laboratories, Burlingame, CA). 3,3′-Diaminobenzidine was used as a chromogen.

Confocal fluorescence light microscopy. Rat and guinea pig lungs were degassed under vacuum, filled with fixative of methanol-chloroform-glacial acetic acid 60:30:10 by volume (29), and submerged in a bath of the same fixative for 2 h, with the meniscus of the liquid column continuous with the trachea maintained at 25 cm above the bath, which we consider to be close to maximal physiological volume (total lung capacity; TLC). The left (unlobated) lung was sliced transversely into three to eight slices ~2–3 mm thick, dehydrated in absolute ethanol, embedded in paraffin, cut ~7 μm thick, deparaffinized by standard techniques, and affixed to slides. For fluorescent staining of α-smooth muscle actin, slides were incubated in 0.1% Triton X-100 in 0.1 M Tris-buffered saline (TBS, pH 7.6) for 10 min, washed in TBS-bovine serum albumin (TBS-BSA) three times for 10 min each, incubated in TBS-BSA containing 1% horse serum for 30 min, incubated in mouse anti-human α-smooth muscle actin antibody (1:100 dilution in TBS-BSA, containing 1% horse serum and 0.1% Tween 20, Sigma Chemical, St. Louis, MO) overnight at 4°C, washed with TBS three times for 10 min each, incubated with biotinylated goat anti-mouse IgG (1:100 dilution with PBS-BSA-HS; Sigma Chemical) for 2 h,

washed in PBS three times for 10 min each, incubated in the dark with ExtraAvidin Cy-3 complex (1:100 dilution with 0.1 M PBS, pH 8.2; Sigma Chemical) for 1 h, and washed in distilled water two times for 5 min each. For fluorescent counterstaining of tissue in general, slides were incubated in 1:40,000 dilution of BODIPY-SE in 0.1 M $NaHCO_3$ (Molecular Probes) for 30 min and washed in distilled water two times for 5 min each.

Transmission electron microscopy. Rat lungs were similarly prepared, except that the intratracheal fixative was 2% paraformaldehyde, 0.1% glutaraldehyde in 0.1 M cacodylate buffer, pH 7.4. The slices, after dehydration in absolute ethanol, were embedded in LR white resin (Polysciences; Warrenton, PA). Ultrathin sections were cut and mounted on gold grids (Polaron Equipment; Watford, UK). Grids were incubated overnight with α-smooth muscle actin antibody as described above, washed, incubated with goat anti-mouse IgG gold (1:40 dilution with the same diluent as used for the primary antibody, Sigma Chemical) for 2 h, washed with TBS-BSA two times for 5 min and then with distilled water two times for 5 min; air-dried overnight; and finally counterstained with uranyl acetate and then lead nitrate.

Imaging and Field of View Selection

Transmission light microscopy. Sections were viewed with a Zeiss Photomicroscope I with ×25 objective, 1.25 intermediate lens. A Dage-MTI CCD video camera fed a signal to a Sony Trinitron monitor and Sony Video Printer. The images on the monitor were ×375 final magnification. Forty-two contiguous, nonoverlapping fields of view covering the entire usable area of the section were acquired.

Confocal fluorescence light microscopy. Sections were examined with ×63 (rat) or ×100 (guinea pig) objectives. The optimal pinhole size in the confocal detection unit was selected so as to collect as much light as possible while still obtaining nearly maximal depth resolution. This depends on the ratio of magnification to numerical aperture. It corresponded to a diameter of 20 μm (rat) or 40 μm (guinea pig) in the image plane of the objective. Cy-3 was excited by a laser light beam at 568-nm wavelength and detected at 620 ± 30 nm (red). BODIPY-SE was excited at 488 nm and detected at 525 ± 25 nm (green). Because of overlap between the Cy-3 and BODIPY-SE images, we used a recently developed adaptation of IMS and morphology-based image processing (see DISCUSSION). The energies and intensity modulations of the two excitation beams were monitored before imaging of each sample. Pixels represented areas 0.32 μm on a side for the rat and 0.2 μm for the guinea pig.

As seen in the raw 620-nm images (Fig. 1*A*), Cy-3 stained large masses of α-smooth muscle actin in the smooth muscle bands in walls of airways and blood vessels and smaller groupings of α-smooth muscle actin in the alveolar ductal structures. Images were processed with the sequence of morphological operations "2× dilate, 4× convex hull creation, 2× erode, and 1× isolated pixel removal" to remove isolated pixels and to collect pixels enfolded by a group of α-smooth muscle actin pixels or between two or more neighboring groups (35). Those pixels preserved after thresholding and

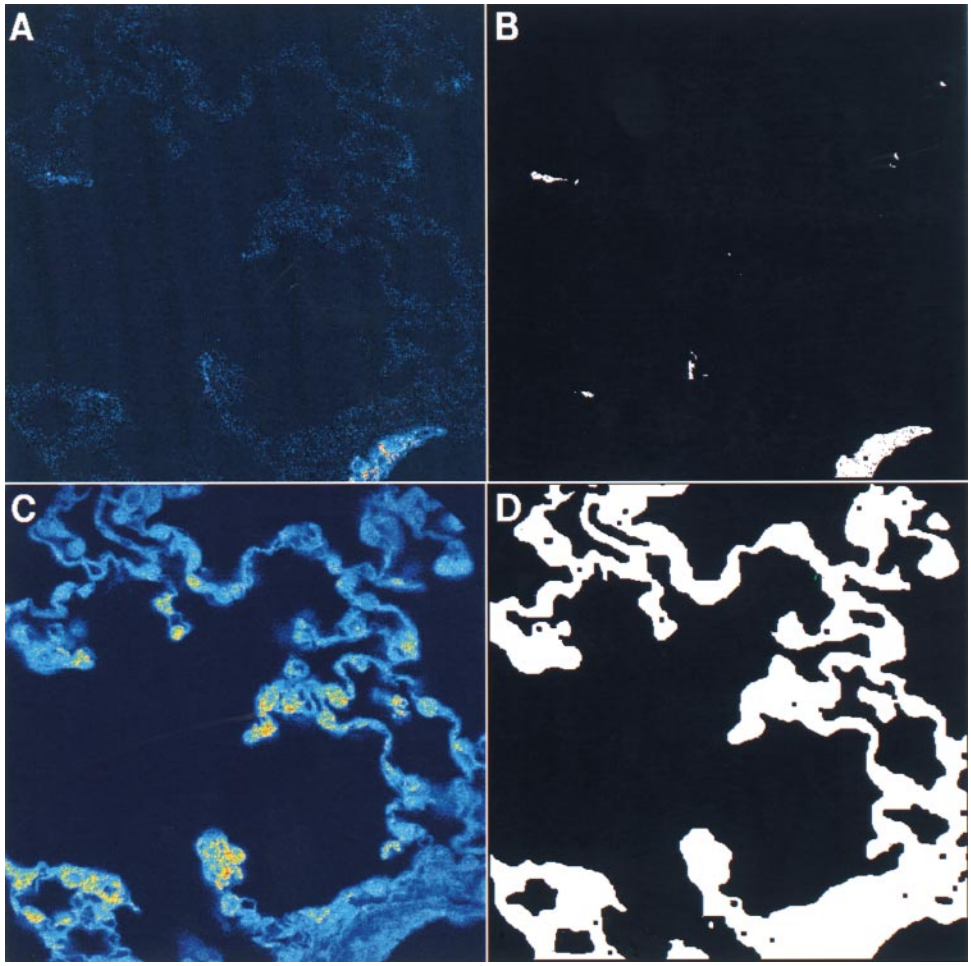

Fig. 1. Four intensity-modulated multiple-wavelength scanning confocal micrographs of the same field of view of a rat lung section. *A*: raw image for Cy-3 immunofluorescence (620 nm). *B*: same image after thresholding and morphology-based image processing. *C*: raw image for BODIPY-SE fluorescence (525 nm). *D*: same image after thresholding and morphology-based image processing. Pixels in *A* and *C* are shown with intensity registered on a color scale. White pixels in *B* and *D* are those selected as α-smooth muscle actin and tissue respectively. Areal densities (Table 2) are obtained from the counts of pixels in *B*, categorized by the anatomical context of *D*.

image processing were considered α-smooth muscle actin (Fig. 1*B*). As seen on the raw 525-nm images (Fig. 1*C*), BODIPY-SE stained all tissue, including α-smooth muscle actin-containing structures. Tissue was readily distinguished from generally dimmer air and lumen pixels by thresholding at an interactively chosen intensity. The same sequence of morphological operations that separated α-smooth muscle actin from tissue on the 620-nm images was also effective on the 525-nm images in smoothing the edges of tissue profiles, filling internal holes due to noise, and repairing occasional gaps in thin capillary wall profiles. Small capillary lumens were also filled, although lumens of arterioles and venules were not, in general. The pixels preserved after this operation (both α-smooth muscle actin- and non-α-smooth muscle actin-containing) were considered tissue (Fig. 1*D*). Each animal generated three to five lung slices. Systematic sampling was performed on a rectilinear grid with constant spacing and random starting point; 2.7 and 1.5% of the areas of the sections of rat and guinea pig lung, respectively, were recorded.

Transmission electron microscopy. Micrographs of sections stained with immunogold were viewed at an instrumental magnification of ×20,000 and were printed at a final magnification of ×68,000. All micrographs from a single animal were of tissue sections stained under the same conditions. Gold particles decorated smooth muscle cells in all airway and blood vessel walls and were very rare in airspaces or vessel lumens, indicating adequate sensitivity and specificity.

Quantifying α-Smooth Muscle Actin in Anatomical Context

We first addressed the quantitative distribution of α-smooth muscle actin among three sites: blood vessels, airways, and alveolar structures. On the confocal fluorescence light micrographs, we identified all airways (terminal bronchioles and larger) on each field-of-view's original image pair by referring principally to the 525-nm channel's images, but also to the 620-nm channel's images for clarification of smooth muscle morphology. A polygon was drawn closely around the airway, and the tissue within was categorized as airway. Analogous images were produced for blood vessel (arterioles, venules, and larger) and unknown regions (recognizable as airway or blood vessel but not further classifiable). All remaining tissue was considered alveolar. All pixels selected as α-smooth muscle actin or non-α-smooth muscle actin in each of these anatomic locations were registered from 790 image pairs from the rats and 240 from the guinea pigs. Areal densities of α-smooth muscle actin or tissue were calculated from the fractions of pixels of each category in each location. For example, the areal density of airway contractile elements (*A*ce) at TLC $[(Ace_{aw}/AL)_{TLC}]$ is the product of the morphometrically observed ratio of the number of pixels recording α-smooth muscle actin in airways to the number of pixels recording lung tissue and the areal density of tissue in the fully distended lung. The latter, being stereologically identical with the corresponding volumetric density, was obtained as the mass density of the lung at TLC divided by the mass density of lung tissue, with the assumptions of 0.067 and 1 g/ml, respectively. The use of summed intensities instead of summed areas did not materially affect the estimates of the quantitative distribution of α-smooth muscle actin. Our measurements of the fraction of muscle in the airway wall by the immunofluorescent IMS technique (0.53/6.9 = 8%; see Table 2) were similar to previous measurements obtained by tracing relevant areas on digitized light micrographs (Table 1 of Ref. 15). This tends to validate our quantitative approach, although the species were not the same.

We next addressed the prevalence of α-smooth muscle actin among alveolar structures. We examined transmission light micrographs using a Richards surgical microscope at four locations of particular mechanical significance (see DISCUSSION). These are *1*) the border of an alveolar septum that abuts two other septa, appearing on section as a three-way septal junction; *2*) the border of an alveolar septum that abuts one other septum, forming a ridge between the two septa and appearing on section as a distinct bend of the septal trace; *3*) the free border of an alveolar septum, as at an alveolar entrance ring, appearing on section as the free end of a septal trace; and *4*) the alveolar septum away from its borders. We identified and circled all the septal ends and bends on each transmission micrograph (the other two locations turned out to have no identifiable α-smooth muscle actin), and recorded each as showing α-smooth muscle actin stain or no stain. When we applied a similar approach to the confocal light micrographs, we obtained data for the septal ends, but could not obtain satisfactory data for the septal bends, because their characteristic configuration was not well enough preserved in these paraffin preparations for secure identification.

To quantify the distribution of α-smooth muscle actin among the septal ends, we examined confocal fluorescence light micrographs from three rats. A polygon was drawn closely around every septal end on each section studied. The transected areas of α-smooth muscle actin in each of 350 septal ends were obtained from the number of α-smooth muscle actin pixels.

The subcellular concentration and configuration of α-smooth muscle actin were studied on transmission electron micrographs of rat lungs. Fields-of-view centering on α-smooth muscle actin-containing material were collected from airway smooth muscle, blood vessel smooth muscle, and septal ends (36, 35, and 33 fields-of-view, respectively). The outlines of all cells tagged with gold particles were emphasized with a fine-pointed marker. Each micrograph was overlaid with a transparent grid with lines spaced at distances equivalent to 0.4 μm. The number of gold particles visible in each grid square was recorded on the grid, and the mean densities (particles per grid square) were calculated.

For examining the visceral pleura, we abandoned the approach of random sampling because of the discreteness of the pleural structure and the frequent stripping of pleura from sections. On two sections of guinea pig lung, we measured pleural thicknesses, α-actin layer thicknesses, and lung slice perimeters, using calipers on light micrographs. From these we calculated the transected areas of pleural tissue, pleural α-smooth muscle actin, and lung.

MODEL

Overview

Our goal was to predict how activation of the contractile elements in each site affects lung distensibility during periodic breathing, specifically the effects on constriction, elastic recoil, and compliance. Our approach was to model a region of lung as an extensive network of elastic elements within which are embedded various contractile structures, namely airways, blood vessels, and alveolar ducts. During breathing, the entire region is cyclically extended and released, and the lengths and tensions of its elastic and contractile components are cycled according to their mechanical properties and their mechanical linkage.

The model respects the important distinction between elasticity and plastoelasticity. We assume that the lung behaves reasonably elastically, i.e., its stress-strain relationship is single valued. By contrast, the activated contractile elements are plastoelastic, i.e., they can change their stress-strain relationship substantially, e.g., after being stretched (11, 14, 39, 42). Although the two systems have this fundamental difference, they are each reasonably predictable.

The model also respects fundamental differences in the mechanical linkage of the elastic and contractile elements. When two elements are linked in parallel, i.e., side by side, their lengths are the same, whereas the net tension is the sum of their individual tensions. By contrast, when they are linked in series, i.e., end to end, their tensions are the same, whereas their lengths sum to the net length. The present context suggests both models. The anatomies of the contractile elements of the pleura and of the axially oriented elements in the airways and blood vessels suggest mechanically parallel linkages with the elastic network of the lung. Because the dimensions of both elastic and contractile components depend only on lung volume, the contributions of each component to lung recoil can be predicted from its characteristic mechanical properties, the level of activation, and lung volume, lung volume excursions, and timing. Their contributions can be simply summed. By contrast, although the circumferentially oriented elastic and contractile elements of the ducts, airways, and blood vessels are mechanically in parallel with each other, they in turn are linked mechanically in series with the surrounding alveolar parenchyma. Because of the series linkage, the activated contractile elements at any given lung volume are shorter; the duct, airway, or vessel is narrower; and the surrounding alveolar parenchyma is drawn in. The governing constraint here is that the additional radial tension due to the contractile element matches the net increase in opposing radial tensions in the elastic structures, i.e., in the surrounding parenchyma and the passive elastic elements of the duct, airway, or blood vessel. Calculations for serial linkage are more complex than for parallel linkage, because the elastic solution must include the distortion from contraction of the embedded structures, and the dimensions and tensions of elastic and contractile components must be resolved to be compatible with each other, with each following its respective properties.

Responses of the Elastic Structure to Internal Contractile Stress

The major assumptions are: *1*) that the noncontractile structure of the lung is linearly elastic over the range of distortion under consideration (22), which includes the airways, blood vessels, and alveolar ducts as well as the network of alveolar septa that surrounds them and does not separate the properties of their different tension-bearing components; *2*) that, for serial linkage, predictions of small deformation elasticity theory are reasonable approximations for the magnitude of deformation of concern; and *3*) that constriction of the alveolar duct is reasonably spherical and that of airways or blood vessels reasonably cylindrical.

Spherical model for constriction of the alveolar duct. Consider a spherical ventilatory unit, comprising a spherical alveolar duct and its associated alveoli. The structural elements of the duct consist of a net of connective tissue "cables" and their accompanying contractile elements. In the model, we replace that spherical net by a thin-walled spherical shell with the same mechanical properties as the net, and we express the radial stress at the interface as a stress jump across the wall of the shell. The contribution of the activated contractile elements to that transmural stress jump (Ptm_{active}) is obtained from the Laplace relationship, in which the contractile tensions are those of passively cycled, activated smooth muscle and the stereologically determined density of α-smooth muscle actin in the unit. The contribution of the passive elements ($Ptm_{passive}$), is taken, for computational purposes, at the radial stress at the surface of a solid spherical elastic continuum that has the same bulk modulus as that of the whole lung (22).

The alveolar network forms a thick-walled spherical shell lying outside the duct. Its mechanical properties are similar to those of the whole lung, on the bases of the relatively homogeneous expansion of the duct and parenchyma during inflation of the relaxed lung (2, 13) and in addition the similarity in shear of the macro and micro strains (4) (*assumption 1*). This thick-walled shell is modeled as an elastic continuum with the same bulk and shear moduli as those of the whole lung (22).

A region of lung comprises a number of such spherical ventilatory units with identical properties. We assume that the small departures of the units from spherical shape to pack them together do not materially change their behavior. When considering a region that is homogeneously activated, we represent the behavior of the whole by the behavior of a single unit.

We first derive the relationship between stress in the contractile elements and constriction of the duct at fixed lung unit volume and then the effects of that constriction on the recoil of the unit. We base the analysis on small deformation elasticity theory for a prestressed elastic structure, the constraint that the radial stresses at the interface between the duct and the surrounding parenchyma remain balanced, and the Laplace relationship. As developed in the APPENDIX, constriction is a function of the elastic moduli, the volumetric density of the relaxed duct relative to its ventilatory unit, and the incremental tension developed by the contractile elements of the alveolar duct

$$(u/a_1)_{duct} = 2(3\kappa + 4\mu)^{-1}(\rho - 1)(\delta T_{duct}/a_1) \qquad (1)$$

The increment in regional lung recoil is a function only of volumetric density and contractile tension

$$\delta P_{L_{duct}} = 2\rho(\delta T_{duct}/a_1) \qquad (2)$$

Eqs. 1 and *2* appear in the APPENDIX as *Eqs. A5* and *A7*.

Cylindrical model for constriction of the airway or blood vessel. The analysis for the cylindrical structures differs from the above in two ways. First, there is an axial linkage to consider. We assume that, because of the treelike structure of the airways and blood vessels, the lengths of airway and blood vessel segments are absolutely constrained by lung volume and vary closely with its cube root, regardless of activation. The linear linkage of the segments suggests that axial tensions can be transmitted along the branches of the trees, independent of the tensions in the alveolar parenchyma. The axial components, thus, are mechanically in parallel with the parenchyma. Second, there is an asymmetry to the serial linkage because at a fixed lung volume the segments can narrow without changing length by drawing in on the surrounding alveolar network. Absent an elastic solution for such a deformation, we take the approach of an earlier report from this laboratory (45) and consider the effects of radial constriction at fixed lung unit volume as a volumetric constriction within an extensive elastic medium.

We consider the effects of circumferential and axial tensions separately. As developed in the APPENDIX, radial con-

striction of the airway (or blood vessel)[1] is a function of the shear modulus and the increment of circumferential tension

$$(u/a_1)_{aw} = -\tfrac{1}{4}\,\mu^{-1}(\delta T_{circ}/a_1) \quad (3)$$

and the increment in regional lung recoil is a function of the elastic moduli, volumetric density, and increments of both circumferential and axial tensions

$$\delta P_{L_{aw}} = (\tfrac{1}{2}\,\kappa/\mu + \tfrac{2}{3})\rho(\delta T_{circ}/a_1) + \tfrac{2}{3}\,\rho(\delta T_{ax}/a_1) \quad (4)$$

Eqs. 3 and *4* appear in the APPENDIX as *Eqs. A11* and *A14*.

Incorporation of stereologic data. The increment of ductal tension is a function of the volume reference for scaling the normal stress of the contractile element, the fractional volume of the lung relative to that at maximal physiological volume, the density of the embedded structures in the lung, and the stereological densities of contractile material.

$$\delta T_{duct}/a_1 = -\tfrac{1}{6}(FRC/TLC)^{-\frac{1}{3}} \times fV_{L_{TLC}}^{-\frac{2}{3}}\rho^{-1}(A_{ce,duct}/A_L)_{TLC}\delta\sigma_{ce,duct} \quad (5)$$

The increments of the circumferential and axial tensions of the airway (or blood vessel) are functions in addition of the angulation of the contractile elements to the axis of the wall segment

$$\delta T_{circ}/a_1 = -\tfrac{1}{2}\sin\theta(FRC/TLC)^{-\frac{1}{3}} \times fV_{L_{TLC}}^{-\frac{2}{3}}\rho^{-1}(A_{ce,aw}/A_L)_{TLC}\delta\sigma_{ce,aw} \quad (6)$$

and

$$\delta T_{ax}/a_1 = -\tfrac{1}{4}\cos\theta(FRC/TLC)^{-\frac{1}{3}} \times fV_{L_{TLC}}^{-\frac{2}{3}}\rho^{-1}(A_{ce,aw}/A_L)_{TLC}\delta\sigma_{ce,aw} \quad (7)$$

Eqs. 5–7 appear in the APPENDIX as *Eqs. A15–A17*. Combining these equations with *Eqs. 1–4* gives the constriction of the duct

$$(u/a_1)_{duct} = \tfrac{1}{3}(3\kappa + 4\mu)^{-1}(FRC/TLC)^{-\frac{1}{3}} \times fV_{L_{TLC}}^{-\frac{2}{3}}(\rho^{-1} - 1)(A_{ce,duct}/A_L)_{TLC}\delta\sigma_{ce,duct} \quad (8)$$

its effect on lung recoil

$$\delta P_{L_{duct}} = -\tfrac{1}{3}(FRC/TLC)^{-\frac{1}{3}} fV_{L_{TLC}}^{-\frac{2}{3}}(A_{ce,duct}/A_L)_{TLC}\delta\sigma_{ce,duct} \quad (9)$$

the constriction of the airway

$$(u/a_1)_{aw} = \tfrac{1}{8}\mu^{-1}\sin\theta(FRC/TLC)^{-\frac{1}{3}} \times fV_{L_{TLC}}^{-\frac{2}{3}}\rho^{-1}(A_{ce,aw}/A_L)_{TLC}\delta\sigma_{ce,aw} \quad (10)$$

the effects of airway constriction on lung recoil

$$\delta P_{L_{aw}} = -(\tfrac{1}{4}\kappa/\mu + \tfrac{1}{3})\sin\theta(FRC/TLC)^{-\frac{1}{3}} \times fV_{L_{TLC}}^{-\frac{2}{3}}(A_{ce,aw}/A_L)_{TLC}\delta\sigma_{ce,aw} \quad (11)$$

and the effects of axial tension on lung recoil

$$\delta P_{L_{aw}} = -\tfrac{1}{6}\cos\theta(FRC/TLC)^{-\frac{1}{3}} \times fV_{L_{TLC}}^{-\frac{2}{3}}(A_{ce,aw}/A_L)_{TLC}\delta\sigma_{ce,aw} \quad (12)$$

Pleural model. In the guinea pig, there is abundant α-smooth muscle actin in the pleura. To estimate its maximal effect on net recoil, we consider a spherical pleura with contractile elements uniformly distributed with regard to location and orientation. As shown in the APPENDIX, pleural tension is the same as is given by *Eq. 5* with ρ = 1, and the effect on lung recoil, then, is the same as that given by *Eq. 9*.

Properties of Passively Cycled, Activated Contractile Element

Like the elastic elements, the contractile element is predictable, although it differs in its substantial plasticity. When activated smooth muscle is cycled, the stress-strain relationship departs dramatically from the classical isometric stress-strain curve depending on the timing and sequence of forces imposed on it. For example, when trachealis muscle is activated maximally at a constant length in vitro, stress rises to a plateau over several minutes. Such plateau values, obtained at different lengths, generate the familiar maximum isometric contraction curve (MICC; Fig. 2, solid curve). If the muscle is forcibly stretched after reaching the plateau tension, stress generally yields along this curve. If it is then shortened rapidly, stress falls sharply away from the MICC. If it is cycled with a frequency and amplitude typical of tidal breathing, it forms a stable, narrow, stress-strain loop that peaks near the MICC but that is much stiffer than the MICC (examples in Fig. 2*A*, dashed and solid loops) (11, 39, 42). Such loops can be generated anywhere along the length axis, creating an infinite array of parallel, narrow, stiff loops.

End-Inspiratory and End-Expiratory Points

For parallel linkage, the lengths follow the cube root of lung volume, the stresses follow the elastic and plastoelastic descriptions, and the recoil is simply the sum of those stresses applied to the appropriate areas. For serial linkage, compatible solutions are required for the elastic and plastoelastic components. In tidal breathing, the elastic structure lies at end-inspiration on its linear function for that volume (*Eqs. 8* or *10*), and the contractile element lies on the MICC. Their intersection identifies the end-inspiratory point. At end-expiration, the elastic structure lies on the linear function for that volume, and the contractile element lies on a curve that comes down from the particular end-inspiratory point of the tidal breath, following the general trajectory of nadirs of such loops (11). Their intersection identifies the end-expiratory point. Applying *Eqs. 9, 11,* and *12*, we obtained the effects on lung recoil. From these data, we can calculate the specific compliances and fractional changes of compliance.

Incorporation of Specific Anatomic and Functional Data

Compatible solutions were found by numerical analysis on a spread sheet (Excel) using *Eqs. 8–12* and curves fitted to the data for volume/pressure, MICC, and the general trajectory of nadirs of repeated loops of activated smooth muscle.

Elastic structure. The isovolume elastic solutions for radius of the airway, vessel or duct, are obtained as $(fV_{L_{TLC}})^{-\frac{1}{3}}(1 + u/a_1)$. The bulk modulus of the lung, κ, is derived from a generalized lung pressure-volume curve (37) and human pressure-volume data (12), and the shear modulus, μ, is derived from lung distortion properties (22) (See APPENDIX). We take fractional FRC (FRC/TLC) as 0.5, and the volumetric densities of the spherical alveolar duct and of the cylindrical airway within their ventilatory units, ρ, as ⅛ and $^1/_{50}$, respectively. The areal density of the contractile element in each location, A_{ce}/A_L, comes from Table 2.

Contractile elements. The MICC is adapted from a generalized curve (Fig. 1, Ref. 47) with maximum stress set at

[1] Parenchymal compliance or inertance in this paper refers to a property directly attributable to tensions in the lung and not to overall behavior that may include important effects due to airway or parenchymal nonuniformities (3, 25).

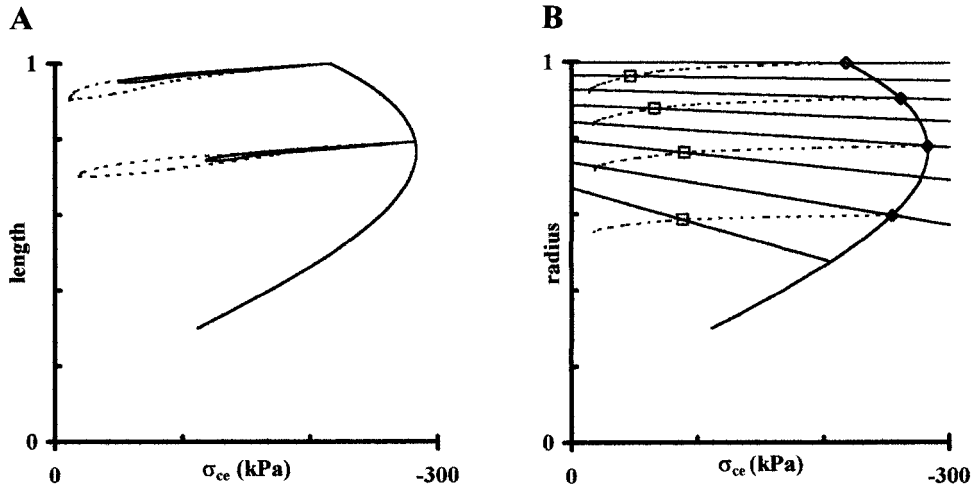

Fig. 2. Effect of activated contractile elements on the elastic structure of the parenchyma during tidal breathing. *A*: typical plastoelastic behavior of the maximally activated contractile element. Length is presented as a fraction of that at total lung capacity (TLC). Nominal stress is referred to the cross-section of the smooth muscle at functional residual capacity (FRC). Solid curve is that for maximal isometric contraction. Dashed and solid loops are for maximally activated smooth muscle undergoing repeated, imposed length cycles of differing amplitude at typical breathing frequencies. Note that, for a given cycling pattern, loops are narrow and stable (i.e., elastic) and are stiff. Nonetheless, different loops form along the maximal isometric contraction curve (MICC) depending on the length to which the contractile element is stretched at the peak of the cycle (i.e., plastic). *B*: superposition of properties of the elastic structure for volumes at intervals of 0.1 of lung fractional volume relative to TLC (fVL_{TLC}) and for a range of contractile element stress (σ_{ce}). Radius is presented as a fraction of that at relaxed TLC and is equivalent to contractile element length. In the absence of contractile stress, radius varies as the cube root of volume, whereas, with increasing contractile stress at fixed volume, elastic modeling (*Eq. 8* or *10*) predicts narrowing (solid line). Trajectories of the nadirs of contractile element strain/stress loops are similar to those in *A* (dashed line). End-inspiratory (◇) and end-expiratory (□) points for tidal breaths between 0.3 and 0.4, 0.5 and 0.6, 0.7 and 0.8, and 0.9 and 1.0 fVL_{TLC} are identified by the intersections of the contractile curves with the isovolume elastic curves as described in the text.

2.88×10^6 dynes cm^{-2} at l_o (15), and with l_o of the relaxed muscle set at FRC. We assume that the length of the relaxed muscle varies as $VL^{1/3}$. A generalized trajectory of end-expiratory points was generated from the end points of a series of dynamic loops (Fig. 1 of Ref. 11), with length scaled in proportion to the length at the end-inspiratory point.

Orientation and closure. The orientation of the contractile elements in the airways is nearly circumferential (23), thus favoring circumferential over axial tension. We modeled the airway with a single θ (77° to the axis of the airway) because the observed distribution is narrow. We did not have information regarding the distribution of θ in the blood vessels, but predictions made with the assumption of uniform distribution of θ (not shown) are not very different. When the airway closes, i.e., when the outside radius falls to ~0.48 of its initial radius (26), any excess of δT_{circ} over that needed for closure has no additional effect on the surrounding parenchyma. We therefore limit the effects of δT_{circ} on recoil (*Eq. 11*) to that threshold. Nonetheless, the full δT_{ax} can still be transmitted along the closed airway tree.

RESULTS

Anatomic Observations

Location. α-Smooth muscle actin appears in the walls of all conducting airways, in the walls of all blood vessels larger than capillaries, and in two of four sites of particular mechanical significance, namely the septal ends and bends, where elastin- and collagen-rich cables are located (34). It is present in about three-quarters of the ends and half of the bends (Fig. 3, Table

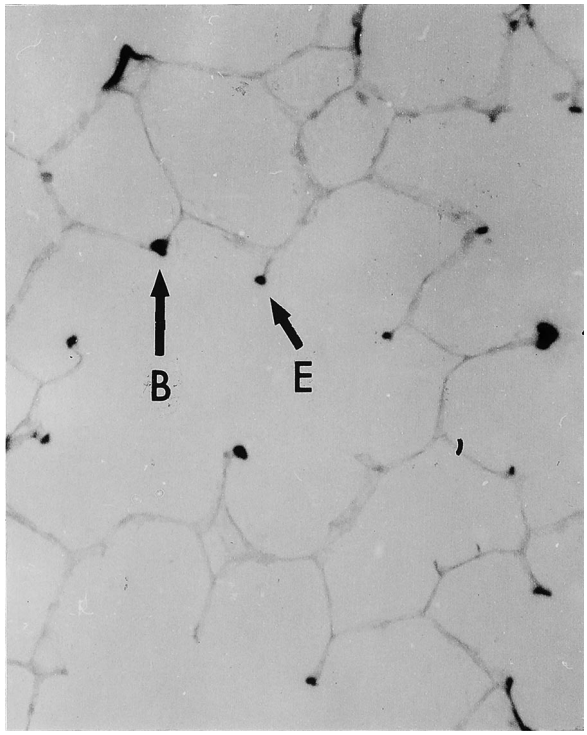

Fig. 3. Light micrograph of rat lung stained by reaction with α-smooth muscle actin antibody, visualized using the immunoperoxidase method. Arrows indicate staining at a typical septal "end" (*E*) and "bend" (*B*).

Table 1. *Prevalence of α-smooth muscle actin in parenchymal cable locations*

	Light Micrography (DAB-HRP)	Confocal Micrography (Cy-3)
Rats		
Ends	0.74	0.75
Bends	0.51	
Guinea pigs		
Ends	0.73	

DAB-HRP, diaminobenzidine-horseradish peroxidase

1). No α-smooth muscle actin was detected in the septa away from the ends and bends, nor in the three-way septal junctions. α-Smooth muscle actin is present in the visceral pleura of the guinea pig, but not in that of the rat.

Quantities. The amounts of α-smooth muscle actin and tissue in the various sites are given in Table 2 and are of roughly similar magnitude in the two species, with the exception of the rat pleura. The rat has slightly less α-smooth muscle actin in the alveolar duct than in either the airways or blood vessels, whereas the guinea pig has more. The rat has more α-smooth muscle actin in its airways and blood vessels than does the guinea pig, but less in the ducts. In addition, the guinea pig has substantial α-smooth muscle actin in the pleura, almost as much as in the parenchyma.

The areas of the individual bundles of α-smooth muscle actin at cable sites as seen on section are mostly 1 μm^2 or less (Fig. 4). The variation of areas is only partly due to tangential sectioning-random sectioning of uniform linear bundles would produce fewer large areas than we saw. It is our impression from the transmission light micrographs that heavier clumps of α-smooth muscle actin are present in clusters of septal ends associated with larger alveolar ducts. In an attempt to confirm this impression, we looked for visual evidence of a gradient of heavy staining from hilum to pleura but were unable to draw a conclusion.

Table 2. *Quantities of α-smooth muscle actin and lung tissue in various sites*

	A_{ce}/A_L (10^{-3})	A_{tiss}/A_L (10^{-3})	$A_{ce}/A_{ce,tot}$
	Rat		
Airways	0.53	6.9	0.31
Blood vessels	0.76	6.1	0.44
Unknown	0.04	2.1	0.023
Alveolar ducts	0.39	51	0.23
Pleura	0	0.31	0
Total	1.7	67	1
	Guinea pig		
Airways	0.28	1.9	0.13
Blood vessels	0.32	3.0	0.15
Unknown	0.08	5.4	0.035
Alveolar ducts	0.84	53	0.39
Pleura	0.66	3.0	0.30
Total	2.2	67	1

A_{ce}/A_L and A_{tiss}/A_L,, areal densities of airway contractile elements and of tissue in the fully distended lung; $A_{ce}/A_{ce,tot}$, fraction of total contractile elements.

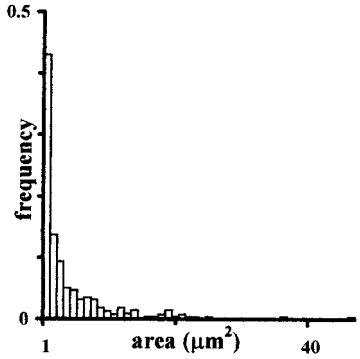

Fig. 4. Frequency distribution of the areas of patches of α-smooth muscle actin seen in septal end structures. Most are <1 μm^2.

Fine distribution and concentrations. At the cellular level, the rat shows distinct differences between the smooth muscle of the airways and blood vessels and the α-smooth muscle actin-containing cells in the cable sites of the alveolar parenchyma. As shown in Fig. 5*A*, the α-smooth muscle actin-containing cells of blood vessels and bronchioles have the well-known morphologic features of smooth muscle: their outline is unbranched, compatible with a fusiform shape; their cytoplasm is nearly filled with electron-dense filamentous material that binds the gold particles; and caveolae are numerous along the cell periphery. The basal lamina in these preparations is not consistently visible, owing to low contrast, but an unfilled gap of several tenths of a micrometer is present between the periphery of neighboring cells or between cells and interstitial fibrils. By contrast, the immunogold-tagged cells in the septal ends (Fig. 5*B*) are represented by profiles of fine cell processes that sometimes branch. The gold particles are bound to packets of electron-dense, filamentous material that occupy a relatively small portion of the profile, the remainder being electron lucent with occasional mitochondria or sacs of endoplasmic reticulum. Caveolae are few, and interstitial fibrils abut the cell periphery, indicating the absence of an intervening basal lamina. These cells indeed resemble the myofibroblasts in other portions of the alveolar wall save for the actin isoform expressed. On the other hand, within the portions of the cells that do contain α-smooth muscle actin, over regions of similar size to the confocal pixels, the concentrations of α-smooth muscle actin (immunogold particles per overlay square) are similar among the ends (1.98) and the smooth muscles of the airways (1.84) and blood vessels (2.02). So, although these cells seem to be myofibroblasts, they appear to have hefty contractile machinery comparable to smooth muscle.

Predictions From Modeling

The end-inspiratory and end-expiratory radii and contractile element stresses during tidal breathing are shown in Fig. 6, *A* and *B*. When relaxed, radii of ducts, airways, and vessels vary simply as the cube root of lung volume, but with activation, the structures are narrower. The degree of narrowing *1*) during a given

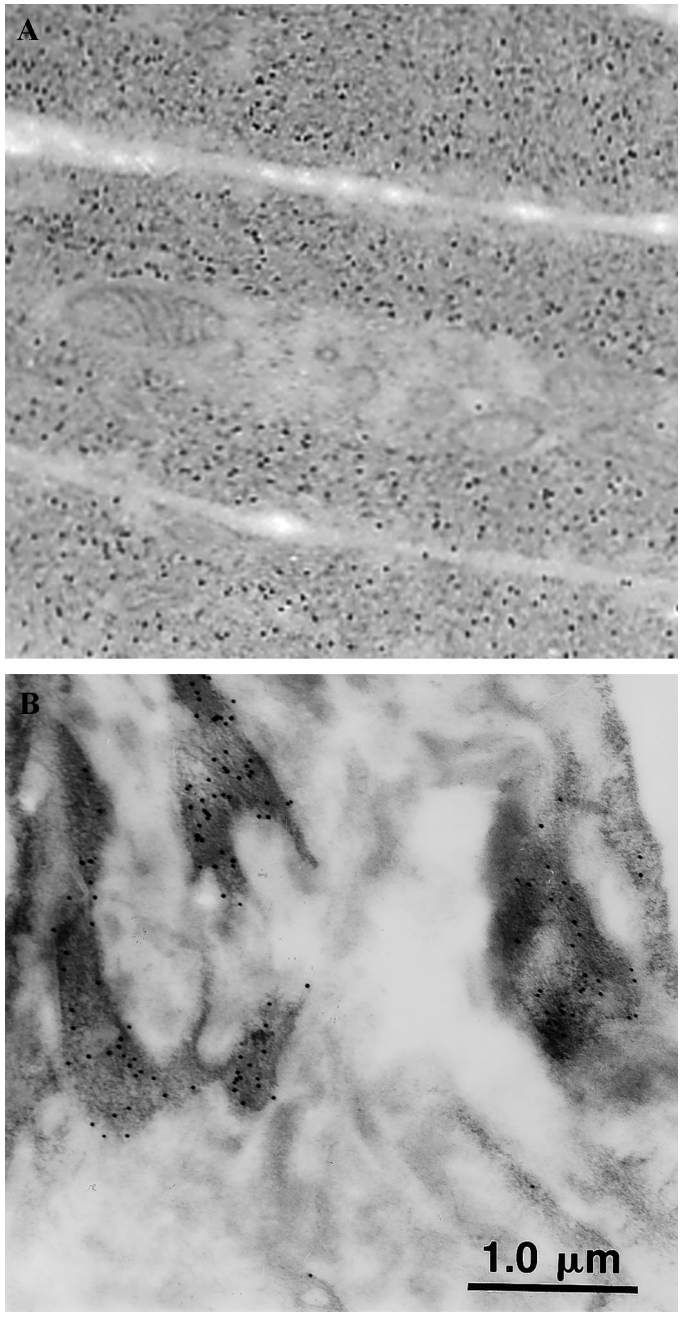

Fig. 5. Electron micrographs of rat parenchyma, contrasting the cells containing α-smooth muscle actin (immunogold-stained) in the airways (*A*) and in the septal end structures (*B*). See text.

tidal breath is greater at end-inspiration than at end-expiration by up to 150%, reflecting the greater contractile stress at end-inspiration; *2*) is generally greater in tidal breaths taken at lower lung volumes, reflecting less opposing tension in the elastic structures; *3*) is greater if the density of α-smooth muscle actin is greater, e.g., the ducts of the guinea pig compared with those of the rat; and *4*) is greater for the airways than for the ducts, reflecting the higher local concentration of α-smooth muscle actin. Maximally activated airways are predicted to close at mid-range lung volumes. Contractile stresses are much lower at end-expiration than at end-inspiration, reflecting the characteristic dynamic stiffness of the activated contractile element. Lung recoil (Fig. 6*C*) is increased modestly, e.g., rat ductal constriction increases recoil by <1 cmH_2O, although this reaches 20% of relaxed recoil at lowest lung volumes. At high lung volumes, the airways have greater effects on recoil than do the ducts. Most of this (about three-quarters, data not shown) is due to circumferential tensions. At lower lung volumes, where the airways close, the contribution of circumferential tension falls off, while that of axial tension increases, reversing the ratio. Specific compliance (Fig. 6, *D* and *E*) is reduced by up to 20–30% with constriction in any one site alone. The effects of pleural activation (guinea pig) on recoil (not shown) were somewhat less than that of ductal activation, but its effects on specific compliance were ~50% greater (Fig. 6*E*).

DISCUSSION

The main findings of this study are *1*) that the amounts of contractile material do not vary widely between the alveolar ducts, airways, and blood vessels of the lung parenchyma, *2*) that estimated effects on lung recoil are small, and *3*) that there is the potential for modest but physiologically significant control of regional compliance.

Methodology

We chose α-smooth muscle actin as a marker of contractile capability, as have others (8). Although the most plentiful isoforms of actin in lung are nonsmooth muscle (24), such isoforms are generally involved in processes (e.g., cell migration, phagocytosis, secretion, and translocation of organelles within the cytoplasm) that do not involve deformation of the tissue external to the actin-containing cell. By contrast, the smooth muscle isoforms are found in cells such as fibroblasts during the contraction of wounds, the myoepithelial cells of gland ducts, and smooth muscle itself, i.e., in sites or circumstances where cells put tension on the surrounding tissue. In addition, the force generated by smooth muscle cells is ~10-fold that generated by contraction of cells such as endothelium and chick embryo fibroblasts with nonmuscle actin (20). We recognize that, in limiting ourselves to the α-smooth muscle isoform, we may have underestimated the intrinsic contractile capability of the alveolar parenchyma. We are not likely, however, to have overestimated it.

We needed images identifying α-smooth muscle actin-containing pixels in anatomical context to quantify contractile elements in the several sites. We had tried several approaches before settling on the described techniques. We failed to obtain reliable immunostaining of α-smooth muscle actin for light microscopy with a number of plastic embedding materials, combined on occasion with etching and removal techniques. Paraffin-embedding provided excellent immunostaining, but DAB-HRP stain deposits were neither well localized nor opaque enough to allow the video microscopic im-

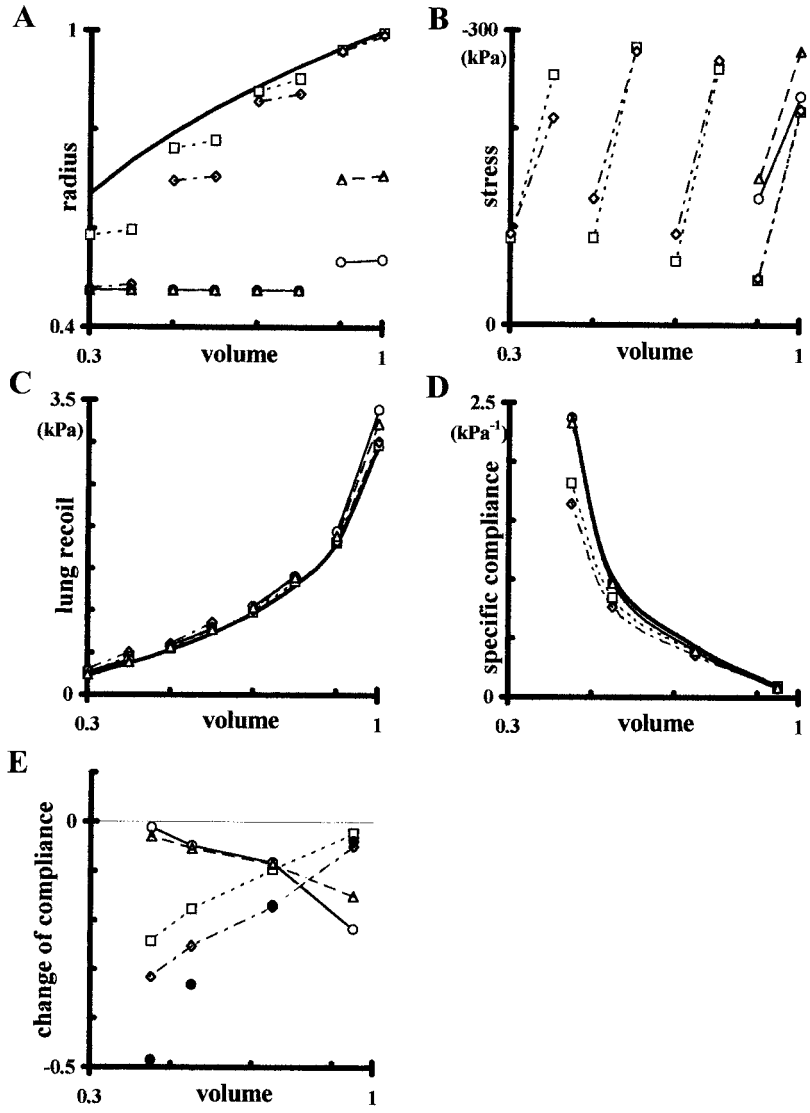

Fig. 6. Predicted effects of activation of contractile elements on the radius of various embedded structures (*A*), on stress in the contractile elements (*B*), on lung recoil (*C*), on specific parenchymal compliance (*D*), and on the fractional change of parenchymal compliance (*E*) during tidal breathing at different levels of inflation. The outer radius of the duct or airway is given relative to its radius at relaxed TLC. Volume is given as fraction of relaxed TLC. Heavy solid lines, relaxed contractile elements; dotted lines and □, activated rat ducts; thin solid lines and ○, rat airways; dot-dashed lines and ◇, guinea pig duct; dashed lines and △, guinea pig airways; ●, guinea pig pleura. See text.

ages to be segmented cleanly into α-smooth muscle actin, tissue, and air regions. We then tried combinations of immunofluorescent staining of α-smooth muscle actin and absorptive or fluorescent staining of tissue, but the thickness of the sections (7–12 μm) meant that portions of the section above and below the plane of focus contributed to both the α-smooth muscle actin and tissue signals, making their separation unreliable. This problem was partly overcome by the use of confocal laser scanning microscopy to look at optical sections that are a fraction of the thickness of the section itself (<1 μm out of 7 μm or more). Nonetheless, even with emission spectra as well separated as those of BODIPY-SE and Cy-3, there was enough cross talk between the two detected signals that separating them quantitatively was insecure. This final limitation was largely overcome by the use of the novel IMS technique (5) in which two lasers are used, each tuned to a suitable excitation wavelength of one of the dyes. The intensities of the two exciting wavelengths are modulated at different frequencies in the megahertz region. As a result, the intensities of the light from the different dyes have different frequencies and can be distinguished by lock-in amplifiers, each tuned to one of the exciting frequencies, rejecting in each case the out-of-frequency signal contaminating that channel. This approach gave us two superimposable images, one showing the α-smooth muscle actin-containing pixels and the other showing lung tissue for context.

The images were further clarified by morphology-based image processing. On the 620-nm image (α-smooth muscle actin), there were individual pixels that appeared to be out of anatomical context. There were two reasons for this. First, tissue pixels are subject to a certain random noise. This is photon quantum noise with a broad frequency spectrum and random signal level proportional to the square root of the signal level of the rejected (525 nm) signal. It randomly increases or decreases the intensity of all tissue pixels, whether α-smooth muscle actin containing or not, creating enough of an overlap of intensity that simple intensity thresholding of the 620-nm channel does not clear it of

the noise from the 525-nm channel. Because the noise is random, however, the severely affected pixels tend to occur in isolation, e.g., isolated low-intensity pixels within typical patches of α-smooth muscle actin and isolated high-intensity pixels in regions of non-α-smooth muscle actin-containing tissue. Second, there were many pixels of equivocal intensity at the borders of patches of α-smooth muscle actin, where many pixels lie partly over α-smooth muscle actin-containing tissue and partly over non-α-smooth muscle actin-containing tissue. These two features (isolation and edges) lend themselves to morphology-based image processing.

Contractile Cells

α-Smooth muscle actin appears not only in classical smooth muscle cells, but also, in the rat, in myofibroblast-like cells (Fig. 5). One of us (C. Kuhn III) has previously found similar cells in the septal ends of mice and hamsters. These cells have concentrations of α-smooth muscle actin at the pixel scale that are comparable to those in smooth muscle. They lie in the same site (alveolar ducts) as do classical smooth muscle cells in the guinea pig, human, and other species (Fig. 3). It seems likely, then, that this cell in this location has a primary contractile function.

Mechanical Linkage-Anatomic Basis

The effect of activation of contractile elements on lung recoil depends on how the contractile and elastic structures of the lung are linked (see MODEL). The outer boundaries of the airway and blood vessel trees deform nearly exactly with the pleural surface, because the relative volume of lung that might be mechanically in series with the trees is a subpleural rim several hundred micrometers in depth, and this is negligible compared with the volume of lung encompassed by the trees. The inner portions of the trees most likely remain shape stable. To the extent that the trees are tensed, branching structures, supported in space by terminal branches, the angles at each branch point are determined by the ratios of axial tensions in the branches and will not change if the axial tensions are changed proportionally during change of lung volume or change in tone. Furthermore, the alveolar parenchyma, within which the tree is embedded, is itself inherently shape stable. Indeed, airways in situ generally change length as the cube root of lung volume, which is completely compatible with shape stability. We conclude that the trees most likely provide a pervasive network that is generally shape stable either with lung volume change or with uniform changes of axial tension in its branches, that the linkage of its axial elements with the lung parenchyma is mechanically in parallel, and that lung recoil is directly changed by changes of axial tensions.

The lengths of the pleural contractile elements (guinea pig only) appear to be tied to lung volume, independent of the elastic elements of the lung, and are thus also in a parallel linkage.

Circumferential elements of the airways, blood vessels, and alveolar ducts, on the other hand, appear anatomically to be linked in series with the elastic structures of the lung. They are situated where they can shorten the elastic elements of the airway or blood vessel at fixed lung volume, drawing in radially on the surrounding alveolar septa, expanding their surfaces and deforming their elastic structures. In particular, the alveolar ductal contractile elements accompany most of the connective tissue "cables" (Table 1), and we presume that their mechanical action is similar. These cables are linear condensations of elastin-rich connective tissue that are positioned to support the free (end) and tented (bend) septal borders by their tensions and curvatures (34, 36) and are not found in the alveolar septa away from the cabled borders or in the three-way septal junctions, where the configurations are simply compatible with locally uniform septal tensions (33). The contractile elements of the duct, then, are positioned to both relieve the elastic elements of the duct and tense the surrounding alveolar network. Presumably this is the mechanism of the dramatic radial constriction of alveolar ducts reported by Nadel et al. (31) in cat lung fixed after barium sulfate embolism. Unfortunately, to date there have been no systematic measurements of the degree and circumstances of such deformation in situ. The tensions of the activated contractile elements in this series linkage goes in part to distort the elastic network and in part to increase the lung recoil. Figure 6, *A* and *C*, shows quantitative predictions of narrowing and change of recoil.

Importance of Incorporating the Dynamic Contractile Properties and the Series Linkage in the Model

The predictions of the model would be very different if we were to ignore the dynamic properties of activated contractile elements and assume instead that the stresses remain high throughout the breathing cycle. In particular, if the stresses in activated rat alveolar ductal elements were to lie on the MICC at end-expiration as well as at end-inspiration, parenchymal compliance would actually increase slightly with activation of the contractile elements (Fig. 7, *curve b*), an unexpected result that relates to the volume-related terms in *Eqs. 9* and *11*. Reduction of parenchymal compliance, then, is largely due to the substantial stiffness shown by the activated contractile element when it is stretched and released at typical breathing frequencies.

The predictions of the model are also different for serial and parallel linkages. For example, a model in which the duct is linked in parallel with the surrounding parenchyma (Fig. 7, *curve a*) predicts greater effects on compliance than our model in which the linkage is serial (Fig. 7, *curve c*). There are two reasons for this. First, in a serial linkage, the relatively stiff activated contractile element has less excursions of length than the excursions required in a parallel linkage (compare the slopes of the four serial linkage curves in Fig. 6*A* with the solid curve which varies as $V^{1/3}$).

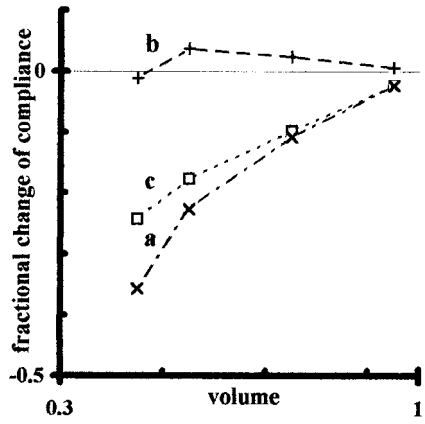

Fig. 7. Comparison of three models. *a*: Parallel (dotted-dashed line, ×). *b*: Constant stress (dashed line, +). *c*: Serial model (dotted line, □). Axes as in Fig. 6*D*. The parallel linkage model overestimates the effect on parenchymal compliance (compare *curves a* and *c*). Dynamic stiffness of the contractile element accounts for virtually all of the predicted reduction in parenchymal compliance (compare *curves b* and *c*).

Therefore it has less excursions of stress. Second, in a serial linkage, the contractile element has less direct purchase on recoil. The parallel model then probably overestimates the effect on parenchymal compliance.

Effects of Activation on Lung Parenchymal Recoil and Compliance

The estimated effects on recoil of activation at each of the sites are generally small (Fig. 6*C*). We were particularly interested, however, in the effects on compliance because of the functional implications to the distribution of ventilation. Contractile stresses are much higher at end-inspiration than at end-expiration (Fig. 6*B*), because of the remarkable stiffness of activated contractile elements when they are length-cycled at typical breathing frequencies (Fig. 2), and, largely for this reason, parenchymal compliance in this dynamic setting is significantly reduced (Fig. 6, *D* and *E*).

Comparison With Previous Theoretical Estimates

A much earlier study from our laboratory had estimated that constriction of the smaller airways could increase lung recoil by as much as 10–20% and had speculated that constriction of more peripheral contractile elements, at the level of the alveolar duct, might have an even greater effect (45). The current report moves well beyond that study in several ways. The earlier estimates, unencumbered by data, were based on an assumption about the fractional narrowing of the airways, whereas we can now base our estimates on measured amounts of contractile material. The earlier study did not attempt to quantify the effects of contraction at the level of the alveolar ducts. It did not address the effects on parenchymal compliance, which is of considerable interest because of its role in distributing ventilation (27) and therefore in modulating gas exchange efficiency (9). Finally, it did not incorporate the stiffness of passively cycled, activated smooth muscle, which turns out in our model to be almost solely responsible for the predicted effects on parenchymal compliance.

Comparison With Experimental Data

Pneumoconstriction has been studied experimentally for decades under a range of experimental conditions: operating lung volumes, volume excursions, frequencies, agents, species, routes of stimulation, and preparations. With major constriction of the conducting airways, the overall dynamic elastance of the lung can increase manyfold (3, 25). Our study finds insufficient contractile material for stiffening the lung parenchyma to that degree and therefore indirectly supports the interpretation that the mechanism of the reported major changes of elastance in those experiments is nonuniformity of airway constriction. Pseudostatic volume/pressure curves, presumably more directly reflective of parenchymal properties, show modest decreases of compliance when agonist is delivered specifically to the bronchi of sheep (30). The magnitudes of these changes are consistent with our predictions for the effects on lung parenchymal compliance. Direct measurements of lung tissue tension in lung tissue strips show contractile behavior with modest increases of tension (7–29%) and changes of dynamic properties that are again generally consistent with the densities of contractile material that we find.

Functional Implications

In the pulmonary vasculature, the accepted role of the smooth muscle is homeostatic redistribution of pulmonary blood flow away from units of low ventilation-perfusion ratio ($\dot{V}/\dot{Q}$). Our analysis suggests an additional effect, which is that narrowing of the vessels would at the same time draw in on the parenchyma, reducing its compliance and redistributing ventilation away from such units. Such an effect would oppose the accepted homeostatic role of pulmonary vasoconstriction on low $\dot{V}/\dot{Q}$ units. This contrary effect, however, is probably very small compared with the homeostatic effect on perfusion because of the exquisite sensitivity of vascular resistance to blood vessel radius.

In the airways, as in the blood vessels, constriction changes flow resistance. In the normal subject, breathing quietly and with minor changes of airway diameter, the changes of flow resistance may do little to the distribution of ventilation because the local time constants are short relative to the period of a breath and therefore the distribution of ventilation is governed primarily by local parenchymal compliance (27). We find sufficient contractile material in the airways or alveolar ducts to bring about significant changes in local parenchymal compliance. This is consistent with the early proposal of Colebatch (6) that alveolar duct constriction enables local control of the distribution of ventilation. The wide distribution of contractile material in the ducts (Table 1) suggests that it could affect relatively small units of lung. To the extent that alveolar ductal elements can be activated independently of

the conducting airways, the distribution of ventilation can be modulated without interfering with other airway functions. Alveolar ductal constriction is predicted to change parenchymal compliance by 20–30% in the volume ranges of quiet breathing (Fig. 6*E*). In healthy humans, lung recoil is reduced and nonuniformity of ventilation is increased after intravenous atropine, suggesting that there is tone in the airways and/or the ducts, defending uniformity of ventilation at baseline (9).

Our predictions for pleural activation represent a maximal effect in that they assume uniform contraction. Such a contraction would seem physiologically disadvantageous given that it would serve only to impose a load (albeit minor) on the muscles of respiration. On the other hand, nonuniform contraction might restrict expansion on one side of a lobe and redistribute ventilation by this means. We can say no more because we have not looked carefully into the distribution and orientation of the pleural elements.

We should caution that our predictions may well overestimate the effect on local lung distensibility because we have not factored in mechanical interdependence of abutting or interconnected lung regions (28). If, on the other hand, several sites were activated at the same time, the effects should be additive. As illustration, Fig. 6*E* shows that, when both airways and alveolar ductal contractile elements are activated at low and mid ranges of lung volume (0.3–0.4 and 0.5–0.6 fV_{LTLC}), parenchymal compliance is reduced by 30% or more.

Perspective

We have applied novel technology to make measurements at a level of lung structure that is very difficult to access for physiological measurements. We find substantial amounts of contractile material in the alveolar duct (where it has long been a structure in search of a function), similar to the amounts in the airways. We estimate that contractile elements in either location could significantly affect parenchymal compliance, and we find that the effect depends almost entirely on the characteristic stiffness of the activated contractile element when it is passively length-cycled at typical breathing frequencies. The reductions in compliance predicted for maximal activation are in the range reported for unilateral pulmonary artery occlusion in dogs and humans. As proposed by Colebatch (6), such local reduction of compliance would benefit gas exchange by reducing the ventilation in high $\dot{V}/\dot{Q}$ regions. Indeed, the response to unilateral pulmonary artery occlusion has been shown to be mediated by hypocapnia, which is an appropriate marker of high $\dot{V}/\dot{Q}$ units. Such hypocapnic lung stiffening has an appealing symmetry with hypoxic pulmonary vasoconstriction in that both poles of the $\dot{V}/\dot{Q}$ spectrum are modulated; i.e., hypoxic pulmonary vasoconstriction increases the $\dot{V}/\dot{Q}$ of low $\dot{V}/\dot{Q}$ units, whereas hypocapnic lung stiffening decreases the $\dot{V}/\dot{Q}$ of the high $\dot{V}/\dot{Q}$ units.

APPENDIX

Spherical Model

To determine radial constriction of the duct, we start with the constraint that the radial stresses must exactly match at the interface between the duct (thin-walled shell) and the surrounding alveolar parenchyma (thick-walled shell)

$$\delta\mathrm{Ppar} = \delta\mathrm{Ptm}_{\mathrm{passive}} + \delta\mathrm{Ptm}_{\mathrm{active}} \qquad (A1)$$

where δPpar is the change of normal stress at the interface due to the local elastic recoil of the surrounding alveolar parenchyma and $\delta\mathrm{Ptm}_{\mathrm{passive}}$ and $\delta\mathrm{Ptm}_{\mathrm{active}}$ are the changes of transmural stress across the thin-walled shell due to the elastic and contractile tensions in the ductal structures. δPpar can be evaluated from the known relations of radial stresses and displacements of the inner and outer boundaries of a thick-walled spherical elastic medium (46). For a fixed outer radius

$$\delta\mathrm{Ppar} = (3\kappa + 4\mu\rho^{-1})\rho(\rho - 1)^{-1}(u/a_1)_{\mathrm{duct}} \qquad (A2)$$

From the bulk modulus and displacement

$$\delta\mathrm{Ptm}_{\mathrm{passive}} = 3\kappa(u/a_1)_{\mathrm{duct}} \qquad (A3)$$

From the Laplace relationship

$$\delta\mathrm{Ptm}_{\mathrm{active}} = 2(\delta T_{\mathrm{duct}}/a_1) \qquad (A4)$$

By combination of these four equations, radial constriction is

$$(u/a_1)_{\mathrm{duct}} = 2(3\kappa + 4\mu)^{-1}(\rho - 1)(\delta T_{\mathrm{duct}}/a_1) \qquad (A5)$$

We can now determine the effects of such constriction on regional recoil, P_L. For spherical geometry, the change of stress at the outer (fixed) boundary of the thick-walled shell, a_2, when the inner boundary is displaced is known (46)

$$\delta P_{L_{\mathrm{duct}}} = (3\kappa + 4\mu)a_1^3(a_1^3 - a_2^3)^{-1}(u/a_1)_{\mathrm{duct}} \qquad (A6)$$

By the geometry of concentric spheres, $\rho = (a_1/a_2)^3$. Combining this with *Eqs. A5* and *A6*

$$\delta P_{L_{\mathrm{duct}}} = 2\rho(\delta T_{\mathrm{duct}}/a_1) \qquad (A7)$$

which is, surprisingly, independent of the elastic properties. *Eqs. A5* and *A7* appear in the text as *Eqs. 1* and *2*.

Cylindrical Model

The analysis for circumferential constriction of the airway (or blood vessel) is parallel to that given above for the spherical model. The change in the radial stress of the surrounding alveolar parenchyma where the outer boundary is remote, i.e., a_2 is large, is given (21) by

$$\delta\mathrm{Ppar} = -2\mu(u/a_1)_{\mathrm{aw}} \qquad (A8)$$

The relaxed bronchial wall has a diameter dependency similar in magnitude to that of local parenchymal recoil (40), and of the opposite sign. Thus

$$\delta\mathrm{Ptm}_{\mathrm{passive}} = 2\mu(u/a_1)_{\mathrm{aw}} \qquad (A9)$$

For the active component, the Laplace relationship for a thin-walled cylinder gives

$$\delta\mathrm{Ptm}_{\mathrm{active}} = \delta T_{\mathrm{circ}}/a_1 \qquad (A10)$$

where δTcirc is the increment in active circumferential wall tension. By combination of *Eqs. A1, A8, A9,* and *A10*

$$(u/a_1)_{\mathrm{aw}} = -\tfrac{1}{4}\mu^{-1}(\delta T_{\mathrm{circ}}/a_1) \qquad (A11)$$

The effect of this constriction on lung recoil differs from the spherical case because, in the immediate environs of a radial constriction of a cylindrical segment, the parenchyma is strained radially, but not axially. We are not aware of an elastic solution for this problem. This anisotropy, however, fades rapidly with distance and can be neglected because the constricting segments are short, sparse, and generally remote from any boundary of interest. We estimate the effect of cylindrical constriction, then, as that of a volumetrically similar spherical constriction, adapting the equation derived in Appendix III of the earlier study (45) to give

$$\delta P_{L_{circ}} = (\tfrac{1}{2}\kappa/\mu + \tfrac{2}{3})\rho(\delta T_{circ}/a_1) \qquad (A12)$$

For the airways (and blood vessel) trees, there is the additional effect of axial tensions, Tax. Their contribution to recoil is $-\frac{1}{3}\rho$ F/A, where F is the axial force and A_{aw} is the cross-sectional area of the airway (45). By geometry, $\delta F/A = -2(\delta T_{ax}/a_1)$. Combining, we obtain the effect of axial tensions

$$\delta P_{L_{ax}} = \tfrac{2}{3}\,\rho(\delta T_{ax}/a_1) \qquad (A13)$$

Summation of *Eqs. A12* and *A13* yields the net effect on lung recoil of increments of active circumferential and axial tensions

$$\delta P_{L_{aw}} = \delta P_{L_{circ}} + \delta P_{L_{aw}} = (\tfrac{1}{2}\,\kappa/\mu + \tfrac{2}{3})\rho(\delta T_{circ}/a_1) + \tfrac{2}{3}\rho(\delta T_{ax}/a_1) \qquad (A14)$$

Equations A11 and *A14* appear in the text as *Eqs. 3* and *4*.

Application of Stereological Data

First, the spherical case, i.e., the alveolar duct. The contractile elements are modeled as an equivalent thin-walled shell. The incremental active wall tension, δT_{duct}, is, from geometrical considerations at an equatorial section, the normal component of the force divided by the length of the equator, $2\pi a_1$. For fibers that lie at an angle, θ, relative to the normal at the equator, the normal component of force is the integral of the normal component of the muscle stress, $-\cos\theta\delta\sigma_{ce,duct}$, times the fiber cross-sectional area. This area is equal to cosθ times the area of fibers observed on the equatorial sectioning plane, $A_{ce,duct}$. Let ρ(θ) be the fractional probability that a contractile element in the wall lies at θ. Its likelihood of being sectioned varies as cos θ, and its area seen on the sectioning plane varies as 1/cos θ. The fraction of the total area seen on section that represents elements lying at θ is thus simply ρ(θ)dθ. For uniform distribution of orientation of the fibers in the plane of the wall, $\rho(\theta) = 2/\pi$. From these relationships, $\delta T_{duct} = -\pi^{-2}\, a^{-1} \int \cos^2\theta\, \delta\theta\, A_{ce,duct}\, \delta\sigma_{ce,duct}$. Integrating over 0 to π/2 and dividing by a_1, we obtain $\delta T_{duct}/a_1 = -[A_{ce,duct}/(4\pi a_1^2)]\delta\sigma_{ce,duct}$.

We can evaluate Ace_{duct} from our stereological data. It is the product of the perimeter of the sphere at its equator, $2\pi a_1$, and its thickness, which in turn is the volume of the wall, $V_{ce,duct}$, divided by its surface area, $4\pi a_1^2$. Thus $A_{ce,duct} = V_{ce,duct}/2a_1$. By geometric considerations, Vce/VL is identical to stereologically obtained $A_{ce,duct}/A_L$, and VL is $^4/_3\pi a_2^3$. Combining, we obtain $A_{ce,duct} = \frac{2}{3}\pi(a_2^3/a_1)\,(A_{ce,duct}/A_L)$.

The radii in this expression depend on the volumetric density of the relaxed embedded structure, ρ, and the fractional volume of the lung unit relative to that at maximal physiological inflation, $fV_{L_{TLC}}$. We take the appropriate reference lung volume for the dimensions of the relaxed smooth muscle as FRC. We restrict the reference dimensions of the contractile element to the relaxed state (designated by the asterisk) in order that we may use published values for nominal stresses developed by smooth muscle. Thus $a_1 = fV_{L_{TLC}}{}^{1/3}\rho^{1/3}a_{2,TLC}$, and $a_1^* = (FRC/TLC)^{1/3}\rho^{1/3}a_{2,TLC}$. The combination of the above equivalencies gives the incremental active tension

$$\delta T_{duct}/a_1 = -\tfrac{1}{6}\,(FRC/TLC)^{-1/3} \times fV_{L_{TLC}}^{-2/3}\rho^{-1}(A_{ce,duct}/A_L)_{TLC}\delta\sigma_{ce,duct} \qquad (A15)$$

Equation A15 appears in the text as *Eq. 5*.

For a spherical pleura investing the lung, the Laplace relationship gives the incremental contribution to the transmural pressure as $2\delta Tpl/a$, where a is the radius. Because the volume contained by the pleura and the lung are the same, $\delta Tpl/a$ is the same as $\delta T_{duct}/a$ given by *Eq. A15* with ρ set at 1.

The cylindrical case for the airways (or blood vessels) parallels the spherical case with the following exceptions. First, whereas we could assume that the contractile elements in the alveolar duct were uniformly distributed in the plane of the network, the smooth muscle in the airways are known to be preferentially oriented. Axial and circumferential tensions, then, vary with cosθ and sinθ, respectively. Second, circumferential tension is the normal force at a sagittal section of an airway segment divided by the length of the segment, l, so *that* $\delta T_{circ}/a_1 = -[A_{ce,aw}/(la_1)]\sin\theta\delta\sigma_{ce,aw}$. Axial tension is the normal force on a transverse section divided by its perimeter, such that $\delta T_{ax}/a_1 = -[A_{ce,aw}/(2\pi a_1)]\cos\theta\delta\sigma_{ce,aw}$. By geometry, Ace_{aw} is the volume of the contractile elements in the wall divided by the perimeter of the cylinder, $V_{ce,aw}/(2\pi a_1)$. The volumetric and areal densities are again identical, but this time the volume of the lung unit is $l\pi a_2^2$. Combining as before, we obtain $A_{ce,aw} = \frac{1}{2}(la_2^2/a_1)\ (A_{ce,aw}/A_L)_{TLC}$. The relevant radii for the cylinder differ in that the inner radius varies with $\rho^{1/2}$ (rather than $\rho^{1/3}$), and thus $a_1 = fV_{L_{TLC}}{}^{1/3}\rho^{1/2}a_{2,TLC}$, and $a_1^* = (FRC/TLC)^{1/3}\rho^{1/2}a_{2,TLC}$. From these equivalencies, the incremental active circumferential and axial tensions are

$$\delta T_{circ}/a_1 = -\tfrac{1}{2}\sin\theta(FRC/TLC)^{-1/3} \times fV_{L_{TLC}}^{-2/3}\rho^{-1}(A_{ce,aw}/A_L)_{TLC}\delta\sigma_{ce,aw} \qquad (A16)$$

and

$$\delta T_{ax}/a_1 = -\tfrac{1}{4}\cos\theta(FRC/TLC)^{-1/3} \times fV_{L_{TLC}}^{-2/3}\rho^{-1}(A_{ce,aw}/A_L)_{TLC}\delta\sigma_{ce,aw} \qquad (A17)$$

Equations A16 and *A17* appear in the text as *Eqs. 6* and *7*.

Elastic Moduli

We invoke the general expression for pressure-volume relationship, $V = V_{max} - (V_{max} - V_o)e^{-KP}$, where V_{max} is the asymptotic volume, K is a shape constant, and V_o is the extrapolated volume at zero pressure (37). The bulk modulus, κ, is the normalized inverse slope of this curve, dP/(dV/V), and, with V_{max} set to 1, is simply $V/[K(1 - V)]$. We take $K = 0.102\ (cmH_2O)^{-1}$, and $V_o = 0.095$ (12). The shear modulus, μ, is 0.7 P (22).

This study was supported by National Heart, Lung, and Blood Institute Grant HL-26863 and by the Swedish Research Council for Engineering Sciences.

REFERENCES

1. **Allgood RJ, Wolfe WG, Ebert PA, and Sabiston DC.** Effects of carbon dioxide on bronchoconstriction after pulmonary artery occlusion. *Am J Physiol* 214: 772–775, 1968.
2. **Ardila R, Horie T, and Hildebrandt J.** Macroscopic isotropy of lung expansion. *Respir Physiol* 19: 102–115, 1974.
3. **Bates JHT, Lauzon AM, Dechman GS, Maksym GN, and Schuessler TF.** Temporal dynamics of pulmonary response to

intravenous histamine in dogs: effects of dose and lung volume. *J Appl Physiol 76*: 616–626, 1994.
4. **Butler JP, Miki H, Squarcia S, Rogers RA, and Lehr J.** Effect of macroscopic deformation on lung microstructure. *J Appl Physiol* 81: 1792–1799, 1996.
5. **Carlsson K, Aslund N, Mossberg K, and Philip J.** Simultaneous confocal recording of multiple fluorescent labels with improved channel separation. *J Microsc* 176: 287–299, 1994.
6. **Colebatch HJH.** The humoral regulation of alveolar ducts. *Airway Dynamics, Physiology, and Pharmacology*, edited by A. Bouhuys. Springfield, IL: Thomas, 1970, p. 169–189.
7. **Colebatch HJH and Mitchell CA.** Constriction of isolated living liquid-filled dog and cat lungs with histamine. *J Appl Physiol* 30: 691–702, 1971.
8. **Collie DDS, Pyrah I, and Watt NJ.** Distribution and quantitation of lung parenchymal contractile tissue in ovine lentivirus-induced lymphoid interstitial pneumonia. Do tissue forces limit lung distensibility? *Lab Invest* 73: 441–447, 1995.
9. **Crawford ABH, Makowska M, and Engel LA.** Effect of bronchomotor tone on static mechanical properties of lung and ventilation distribution. *J Appl Physiol* 63: 2278–2285, 1987.
10. **Dohlnikoff M, Morin J, and Ludwig MS.** Human lung parenchyma responds to contractile stimulation. *Am J Respir Crit Care Med* 158: 1607–1612, 1998.
11. **Fredberg JJ, Inouye D, Miller B, Nathan M, Jafari S, Raboudi SH, Butler JP, and Shore SA.** Airway smooth muscle, tidal stretches, and dynamically determined contractile states. *Am J Respir Crit Care Med* 156: 1752–1759, 1997.
12. **Gibson GJ, Pride NB, Davis J, and Schroter RC.** Exponential description of the static pressure-volume curve of normal and diseased lungs. *Am Rev Respir Dis* 119: 799–811, 1979.
13. **Gil J, Bachofen H, Gehr P, and Weibel E.** Alveolar volume-surface area relation in air- and saline-filled lungs fixed by vascular perfusion. *J Appl Physiol* 47: 990–1001, 1979.
14. **Gunst SJ.** Contractile force of canine airway smooth muscle during cyclical length changes. *J Appl Physiol* 55: 759–769, 1983.
15. **Gunst SJ and Stropp JQ.** Pressure-volume and length-stress relationships in canine bronchi in vitro. *J Appl Physiol* 64: 2522–2531, 1988.
17. **Ingenito EP, Mark L, Lily C, and Davison B.** Autonomic regulation of tissue resistance in the guinea pig lung. *J Appl Physiol* 78: 1382–1387, 1995.
18. **Ingram RH Jr.** Effects of airway versus arterial CO_2 changes on lung mechanics in dogs. *J Appl Physiol* 38: 603–607, 1975.
19. **Kapanci Y, Assimacopoulos A, Irle C, Zwahlen A, and Gabbiani G.** "Contractile interstitial cells" in pulmonary alveolar septa: a possible regulator of ventilation-perfusion ratio? *J Cell Biol* 60: 375–392, 1974.
20. **Kolodney MS and Wysolmerski RB.** Isometric contraction by fibroblasts and endothelial cells in culture: a quantitative study. *J Cell Biol* 117: 73–82, 1992.
21. **Lai-Fook SJ.** A continuum mechanics analysis of pulmonary vascular interdependence in isolated dog lobes. *J Appl Physiol* 46: 419–429, 1979.
22. **Lai-Fook SJ, Wilson TA, Hyatt RE, and Rodarte JR.** Elastic constants of inflated lobes of dog lungs. *J Appl Physiol* 40: 508–513, 1976.
23. **Lei M, Ghezzo H, Chen MF, and Eidelman DH.** Airway smooth muscle orientation in intraparenchymal airways. *J Appl Physiol* 82: 70–77, 1997.
24. **Low RB, Woodcock-Mitchell J, Evans JN, and Adler KB.** Actin content of normal and of bleomycin-fibrotic rat lung. *Am Rev Respir Dis* 129: 311–316, 1984.
25. **Lutchen KR, Hantos Z, Petak F, Adamicza A, and Suki B.** Airway inhomogeneities contribute to apparent lung tissue mechanics during constriction. *J Appl Physiol* 80: 1841–1849, 1996.
26. **Martin HB and Procter DF.** Pressure-volume measurements in dog bronchi. *J Appl Physiol* 13: 337–343, 1958.
27. **Mead J.** Mechanical properties of lungs. *Physiol Rev* 41: 281–330, 1961.
28. **Mead J, Takishima T, and Leith DE.** Stress distribution in lungs: a model of pulmonary elasticity. *J Appl Physiol* 28: 596–608, 1970.
29. **Mitchell D, Ibrahim S, and Gusterson BA.** Improved immunohistochemical localization of tissue antigens using modified methacarn fixation. *J Histochem Cytochem* 33: 491–495, 1985.
30. **Mitzner W, Blosser S, Yager D, and Wagner E.** Effect of bronchial smooth muscle contraction on lung compliance. *J Appl Physiol* 72: 158–167, 1992.
31. **Nadel JA, Colebatch HJH, and Olsen CR.** Locations and mechanisms of airway constriction after barium sulfate microembolism. *J Appl Physiol* 19: 387–394, 1964.
32. **Nagase T, Matsui H, Aoki T, Ouchi Y, and Fukuchi Y.** Lung tissue behavior in the mouse during constriction induced by methacholine and endothelin-1. *J Appl Physiol* 81: 2373–2378, 1996.
33. **Oldmixon EH, Butler JP, and Hoppin FG Jr.** Dihedral angles between alveolar septa. *J Appl Physiol* 64: 299–307, 1988.
34. **Oldmixon EH, Butler JP, and Hoppin FG Jr.** Lengths and topology of alveolar septal borders. *J Appl Physiol* 67: 1930–1940, 1989.
35. **Oldmixon EH, Butler JP, and Hoppin FG Jr.** Semi-automated measurement of true chord length distributions and moments by video microscopy and image analysis. *J Microsc* 175: 60–69, 1994.
36. **Oldmixon EH and Hoppin FG Jr.** Distribution of elastin and collagen in canine lung alveolar parenchyma. *J Appl Physiol* 67: 1941–1949, 1989.
37. **Salazar G and Knowles JH.** An analysis of pressure-volume characteristics of the lungs. *J Appl Physiol* 19: 97–104, 1964.
38. **Salerno FG, Kurosawa H, Eidelman DH, and Ludwig MS.** Characterization of the anatomical structures involved in the contractile response of the rat lung periphery. *Br J Pharmacol* 118: 734–740, 1996.
39. **Sasaki H and Hoppin FG Jr.** Hysteresis of contracted airway smooth muscle. *J Appl Physiol* 47: 1251–1262, 1979.
40. **Sasaki H, Hoppin FG Jr, and Takishima T.** Peribronchial pressure in excised dog lungs. *J Appl Physiol* 45: 858–869, 1978.
41. **Severinghaus JW, Swenson EW, Finley TN, Lategola MT, and Williams J.** Unilateral hypoventilation produced in dogs by occluding one pulmonary artery. *J Appl Physiol* 16: 53–61, 1961.
42. **Shen X, Wu MF, Tepper RS, and Gunst SJ.** Mechanisms for the mechanical response of airway smooth muscle to length oscillation. *J Appl Physiol* 83: 731–738, 1997.
43. **Simon BA, Tsuzaki K, and Venegas JG.** Changes in lung mechanics and ventilation distribution after unilateral pulmonary artery occlusion. *J Appl Physiol* 82: 882–891, 1997.
44. **Skalli O, Ropraz P, Trzeciak A, Bensonona G, Gillesson D, and Gabiani G.** A monoclonal antibody against α smooth muscle actin: a new probe for smooth muscle differentiation. *J Cell Biol* 103: 2787–2796, 1986.
45. **Smith JC, Butler JP, and Hoppin FG Jr.** Contribution of tree structures in the lung to elastic recoil. *J Appl Physiol* 57: 1422–1429, 1984.
46. **Sokolnikoff IS.** *Mathematical Theory of Elasticity*. New Delhi: Tata McGraw-Hill, 1974.
47. **Stephens NL and Hoppin FG Jr.** Mechanical properties of airway smooth muscle. *Handbook of Physiology. The Respiratory System. Mechanics of Breathing.* Bethesda, MD: Am. Physiol. Soc., 1986, sect. 3, vol. III, pt. 1, chapt. 17, p. 263–276.
48. **Swenson EW, Finley TN, and Guzman SV.** Unilateral hypoventilation in man during temporary occlusion of one pulmonary artery. *J Clin Invest* 40: 828–835, 1961.
49. **Swenson ER, Graham MM, and Hlastala MP.** Acetazolamide slows matching after changes in regional blood flow. *J Appl Physiol* 78: 1312–1318, 1995.
50. **Yuan H, Ingenito EP, and Suki B.** Dynamic properties of lung parenchyma: mechanical contributions of fiber network and interstitial cells. *J Appl Physiol* 83: 1420–1431, 1997.